Microstructure, Mechanical Properties and Biocompatibility of Laser Metal Deposited Ti-23Nb Coatings on a NiTi Substrate

Yaojia Ren [a], Jingguang Du [a], Bo Liu [b,**], Z.B. Jiao [c], Yingtao Tian [d], Ian Baker [e], Hong Wu [a,*].

[a] *State Key Laboratory of Powder Metallurgy, Central South University, Changsha 410083, PR China;*

[b] *Department of General Surgery, The Second Xiangya Hospital, Central South University, Changsha, 410011, PR China;*

[c] *Department of Mechanical Engineering, The Hong Kong Polytechnic University, Hong Kong, China*

[d] *Engineering Department, Lancaster University, Lancaster LA1 4YW, United Kingdom;*

[e] *Thayer School of Engineering, Dartmouth College, Hanover, NH 03755-8000, USA.*

* *Corresponding author.*

** *Corresponding author.*

E-mail addresses: hwucsu@csu.edu.cn *(H. Wu),* liubomri@csu.edu.cn *(B. Liu).*

Abstract

To simultaneously obtain superior superelasticity and biological properties, single- and multi-layer Ti-23Nb coatings were deposited on a cold-rolled NiTi substrate using laser metal deposition (LMD). The microstructure of the single-layer coating consisted of a cellular structure with a grid size of ~300 μm in the eutectic layer, strip structures and prior β-(Ti, Nb) phases surrounded by the Ti_2Ni(Nb) phase in the Ni diffusion zone. In contrast, the microstructure of the multi-layer coating consisted of α′, α″, and prior β phases, which arise from the partition of Nb. Compared with the NiTi substrate, the Ni ion release concentration of the single-layer coating is reduced by 45% with similar nano-mechanical behavior, i.e. a nanohardness, H, of ~4.0 GPa, a reduced Young's modulus, E_r, of ~65 GPa, an elastic strain to failure, H/E_r, of ~0.06, a yield stress, H^3/E_r^2, of ~0.016 GPa, and a superelastic strain recovery, η_{sr}, of ~0.3. The reduction of Ni ion concentration for multi-layer coating after 35 days is even better at up to 62%, but at the cost of a degradation in the mechanical properties. The LMD coatings have a high dislocation density, and their creep is controlled by dislocation movement.

Keywords:
Laser metal deposition, Ti-Nb coating, metastable phase, creep, Nickel ion release.

1. Introduction

Human bone is an organized, dynamic and metabolically-active natural composite that exhibits super-elastic properties under cyclic loading [1, 2]. The recoverable strain of human vertebral trabecular bone can reach ~1.13% after 138 cycles (failure cycle) [3]. For mature bone, the elastic modulus and tensile yield strength show a monotonic reduction with aging (~2% decrease per decade), leading to a substantial increase in fatigue fracture of bones in the elderly [4, 5]. Due to their superior damping capacity, super-elastic materials are highly recommended for orthopedic load-bearing implants since they permit a reduction in the local stress intensity. Since the invention of nickel-titanium alloys, they have been used in various biomedical applications, such as endoscopes [6], orthopedic wires [7], and anastomotic rings [8]. However, nickel has proven to be a serious health hazard [9]. Accumulation of nickel in the body through chronic exposure to Ni-containing superelastic alloys can lead to Ni hypersensitivity and contact dermatitis [10, 11]. In order to take advantage of superelasticity but avoiding the Ni sensitivity issues, development of Ni-free biomedical superelastic alloys has become a research hot spot in recent years [12, 13].

Although a number of Ni-free titanium alloys (such as Ti-22Nb-6Zr [14], Ti-15Nb-4Mo [15], and Ti-30Zr-8Nb-2Sn [16]) have been successfully demonstrated, the typical strain recovery of those new alloys is only ~3% owing to the small lattice distortion during the martensitic transformation (β↔α″) [17], while the stress-induced reversible martensitic transformation (B2↔B19′) in NiTi can result in a strain recovery up to ~8% [18]. This level of strain recovery is still far away for Ni-free titanium alloys.

Thus, substitution for NiTi alloys for medical implants and other applications of Ni-free titanium alloys are rather limited at present. One way to reduce the toxicity caused by long-term exposure to nickel is to deposit an inorganic biological coatings (such as TiO_2 [19], hydroxyapatite [20], and bioglass coating [21]) on the NiTi alloy surface, so that the dissolution of Ni ions into human body is prevented. However, such inorganic coatings do not have the capacity to match the superelasticity of the NiTi substrate and therefore will have the risk of cracking during service and releasing Ni^{2+} from the substrate[22]. Currently, NiTi alloys are still the primary choice of superelastic alloys in a wide range of biomedical materials [23]. Recently, it has been found that the addition of Nb can improve the transition hysteresis and biocompatibility of NiTi alloys [24, 25]. A series of NiTi-Nb eutectic materials with outstanding mechanical properties have been developed, showing great potential for replacing binary NiTi alloys [26, 27], that is, using Nb instead of Ni to alleviate the impact of nickel exposure as much as possible without compromising material properties.

A promising solution to take advantage of superelastic NiTi material while avoiding the unreliable inorganic coatings is to apply a thick layer of a strong and coherent TiNb coating on a NiTi substrate using laser metal deposition (LMD). LMD uses coaxial powder feeding accompanied by *in-situ* laser melting and has been applied extensively in coating preparation [28-30]. This technology is also known as a 3D printing technology, which is capable of producing 3D components layer by layer. Because the metallic powders are completely melted by the laser beam, they have excellent bonding to the substrate and a low diffusion from the substrate [31]. Therefore,

Ti-Nb coatings deposited on a NiTi substrate are proposed here to improve the biocompatibility while preserving the substrate's superelasticity.

During the laser melting process, the peak temperature of the molten pool can reach over 3000 K, after which the liquid metal undergoes ultra-fast cooling of 10^2 - 10^4 K/s. The latter quenching is followed by a cyclic re-heating due to consecutive deposition in adjacent layers [32-34]. Because of this thermal history, hierarchical heterogeneous microstructures at different length scales are formed [35, 36].

The molybdenum equivalency (Mo_{eq}) reflects the capability of an alloying element to stabilize the β phase. It is calculated from Mo_{eq} = 0.28Nb in Ti-*x*Nb binary alloys (*x* refers to Nb concentration in weight percentage, wt.%). When the calculated Mo_{eq} value is larger than 10 wt.%, the metastable β phase can be retained at ambient temperature [37, 38]. Recent studies have confirmed that the Ti-*x*Nb ($x \geq$34 wt.%) alloys produced by selective laser melting (SLM) are dominated by coarse columnar β grains [39, 40]. Nano-scale elemental segregation, which is inevitable in additive manufacturing, may promote the formation of metastable phases, e.g. α′, α″. For example, the α′ martensite phase is enriched in vanadium in SLM Ti-6Al-4V alloys [41, 42]. The thermal cycling in SLM processing may induce *in-situ* decomposition of the metastable α′ phase [43, 44], as the consecutive laser melting in neighboring area heats the material. Although the peak temperature during this cyclic heating can exceed the martensite transformation temperature (*M*s), for less than five thermal cycles decomposition of the metastable phases and recrystallisation may only occur to a trivial extent, and therefore can be largely ignored [45]. The exact microstructure of Ti-23Nb coatings (at.%, 36.7

wt.%) produced by LMD remains unclear, particularly in the presence of Ni diffusion from the substrate.

The deformation of human bone under a static load for a prolonged period is a time-dependent irreversible process. This kind of micro-deformation (i.e. creep deformation) is the precursor for the formation of bone cracks. The ability to inhibit creep deformation is regarded as one of the critical indicators for medical implants [46]. It is quite difficult to investigate the creep behavior of thin coatings through traditional uniaxial tension or compression tests. As an effective and non-destructive method to evaluate the deformation behavior, nanoindentation has been progressively applied in recent years [47-49]. However, the creep behavior of LMD TiNb coatings has rarely been reported.

In this study, both single- and multi-layer Ti-23Nb coatings were deposited on NiTi substrates using LMD, and the microstructural evolution, nanomechanical properties, and creep behavior between substrate and coatings were systematically investigated. Nickel ion release tests of the substrate and coatings were also performed.

2. Experimental

Single- and multi-layer Ti-23Nb (at.%) coatings were successfully deposited onto a cold-rolled Ni-49Ti substrate (at.%) using an LMD machine equipped with an MFSC-500W fiber laser system (Maxphotonics Inc., China). Multi-layer coatings were produced by repeating three single-layer processes to minimize the solid-solid phase transformations. The actual composition of the coatings was 22.51 Nb and 77.49 Ti

(at.%), measured through inductively coupled plasma mass spectrometry (ICP-MS, Thermo, USA). The laser power, scanning speed and layer thickness were set at 350 W, 2.0 mm s^{-1} and 500 μm, respectively. The processing was performed under flowing high-purity argon with a flow rate of 25 L min^{-1}. Details of other processing conditions are described elsewhere [50].

The microstructures of the coatings were examined using a scanning electron microscope (SEM, FEI Quanta FEG 250). A transmission electron microscope (TEM, FEI Talos F200X), operated at an acceleration voltage of 200 kV and equipped with an energy dispersive X-ray spectroscopy (EDS) detector, was used to further characterize the phase constituents. Selected area electron diffraction (SAED) was used to determine the phases present and their orientation relationships. The elemental distribution was examined using EDS in STEM mode.

The nanohardness (H) and reduced Young's modulus (E_r) were obtained by the conventional Oliver-Pharr method using an Ultra Nano Hardness Tester (UNHT) with a Berkovich indenter [51]. A peak load of 40 mN was applied at 60 mN/min and held for 15 s after reaching the maximum value. Each measurement was repeated at least 5 times to ensure the consistency of data. For room temperature creep tests, the load-holding time was extended to 600 s.

To examine the Ni ion release, coated samples were cut into 1 cm^2 squares and cold mounted in epoxy resin to only expose the defined area. The samples were then immersed in 4 ml of simulated body fluid (SBF) at 310 K. The nickel ion concentration of the different samples was detected after immersion for 1, 7, 14, 21, 28, and 35 days

using ICP-MS of the liquid. The nickel ion concentration per square centimeter (C_N) was extracted from the released nickel ion mass divided by the exposed area, *S,* i.e. $C_N = m/S = nV/S$, where *n* is the nickel ion concentration and *V* is the volume of the solution (4 ml).

3. Results

3.1 Microstructure evolution of Ti-23Nb coatings produced by LMD

Figure 1 shows secondary electron (SE) images of the single- and multi-layer Ti-23Nb coating produced by LMD. Figure 1a is a side view image of the single-layer coating, which consists of three parts: NiTi substrate, eutectic layer and Ni diffusion zone. Figure 1b is an enlarged view from Fig. 1a. The eutectic cellular network with a grid size of ~300 μm can be observed. It is clear that fine spherical particles are formed at the cells boundary, and finally grow into dendritic structure away from eutectic layer, as marked by arrows. The top-view of the single-layer coating (Fig 1c) presents a similar result compared with Fig. 1a, with the coexistence of both cellular and dendritic structure. Without the influence of Ni diffusion, the prior equiaxed β grains of multi-layer coating can be observed, as shown in Fig. 1d. There are obvious metastable phases perpendicular (marked in Fig. 1d) to each other inside the grains.

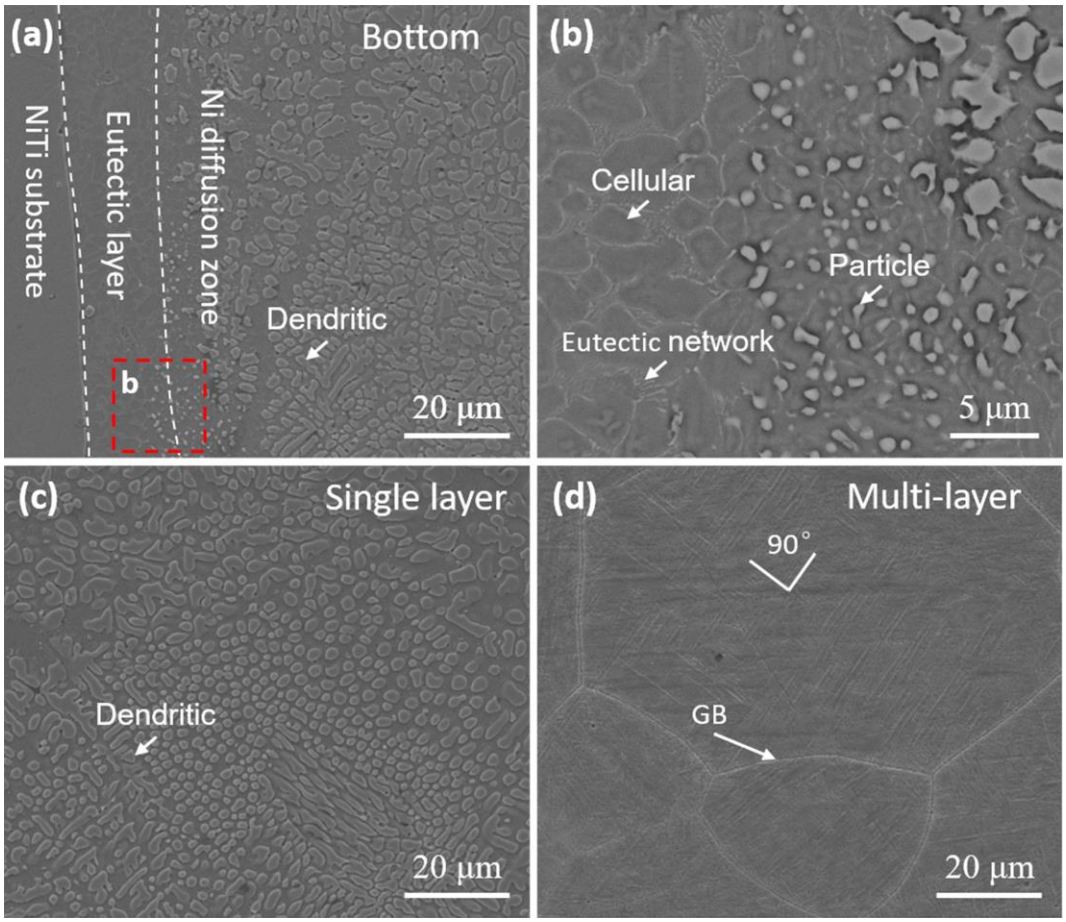

Fig. 1. SE images of LMD Ti-23Nb coatings: side-view image of (a) single-layer coating, an enlarged view of area b in (a); top-view images of (c) single-layer and (d) multi-layer coatings.

The bright-field (BF) TEM image in Fig. 2 shows the fine details observed in eutectic cellular network. It shows a complex morphology which is dominated by β-(Ti,Nb) cellular structures (~100 nm) with rod-shaped phase precipitates in a NiTi(Nb) matrix. The EDS point analysis from P1 and P2 clearly shows that the Ni-containing matrix is enclosed by Nb-enriched precipitates. A HRTEM image of rod-shaped β-(Ti,Nb) phase (~20 nm width) and corresponding enlarged HRTEM of area c are shown in Figs. 2b and c. It shows that the interplanar spacing for the (110) plane is 0.233 nm

for the β-(Ti,Nb) phase and 0.226 nm for the NiTi(Nb) phase. A high density of misfit dislocations exists on the phase boundary (PB) due to the lattice mismatch. An SAED pattern from the β-(Ti, Nb) phase highlighted in Fig. 2b is shown in Fig 2d. The pattern is consistent with a BCC crystal structure viewed along <110>.

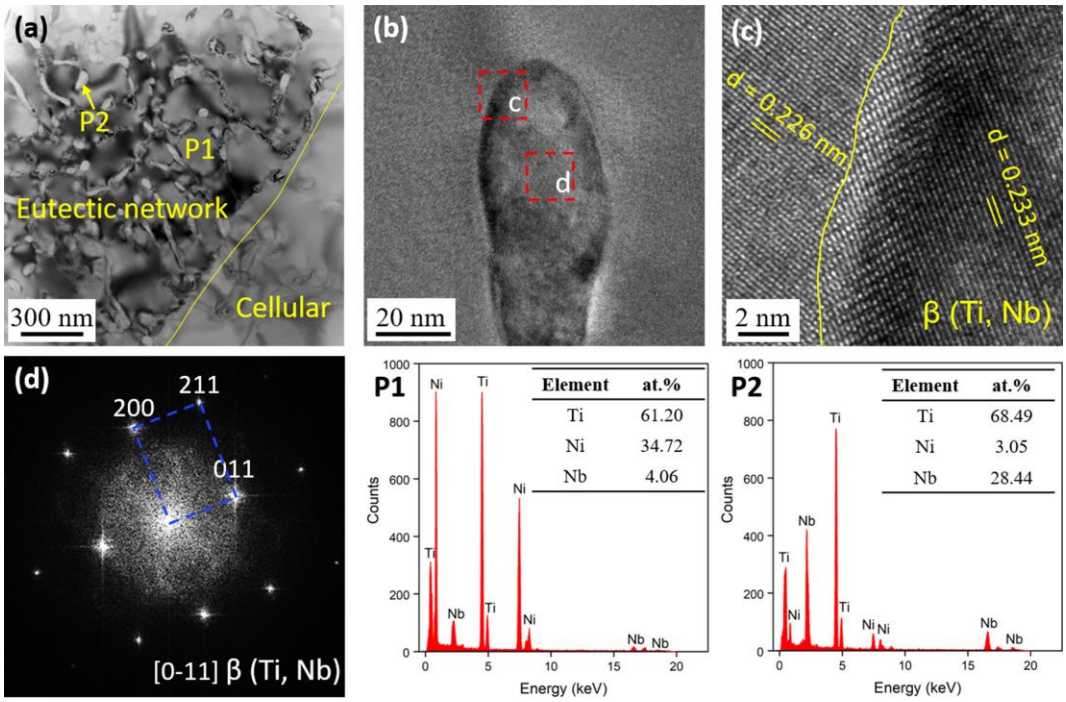

Fig. 2. (a) BF-TEM image taken from eutectic layer; (b) HRTEM image of eutectic cellular network; (c) HRTEM image of the PB between NiTi(Nb) and β-(Ti, Nb), an enlarged view of area c in (b); SAED pattern along [0-11] β zone-axis; P1 and P2 are the corresponding EDS point analysis results.

The TEM images in Fig. 3 present the microstructure taken from the Ni diffusion zone. It is evident in Fig. 3a that high melting point solutes (Nb-rich) are first precipitated as primary β-(Ti, Nb). They are approximately 500 nm in diameter. Figure 3b, an enlarged view of area b in Fig. 3a, shows a BF image of the primary β-(Ti, Nb) and the Ti_2Ni(Nb) matrix. The corresponding SAED patterns in S1 and S2 show the

BCC phase (precipitates) viewed along [001] and the FCC phase (matrix) viewed along [-114], respectively. The PB between the precipitates and matrix is shown in Fig. 3c. Of particular interest is that the strip structure in Fig. 3d (an enlarged view of area d in Fig. 3a) is formed near the primary β-(Ti, Nb) phase. The width of transition zone between these two phases is approximately ~250 nm. The EDS mapping results for Nb and Ni given in Fig. 3a indicate that the formation of aforementioned Ti_2Ni(Nb) matrix in the transition zone is depleted in Nb. The solidification process is dominated by thermodynamics in this case. Away from the transition zone, the concentration of nickel and niobium reaches equilibrium again, i.e. the melt forms the eutectic strip structure upon solidification.

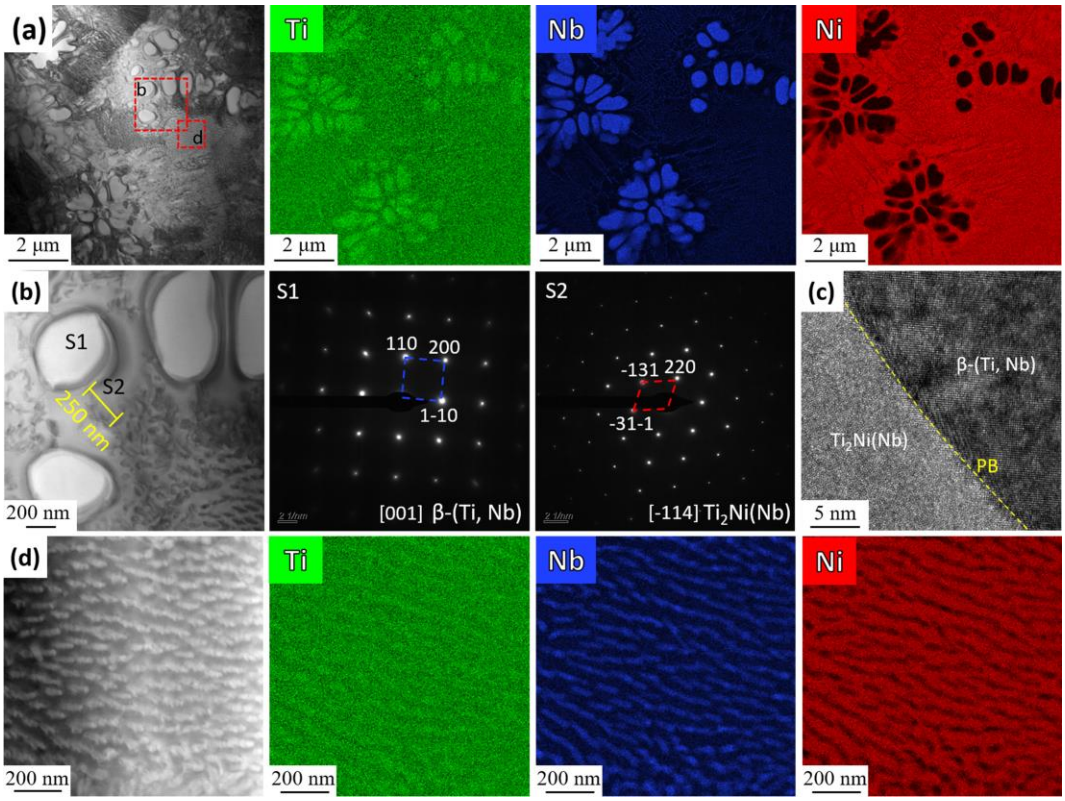

Fig. 3. BF-TEM image taken from (a) the Ni diffusion zone and corresponding STEM-EDS elemental maps; (b) BF image of the primary β-(Ti, Nb) and Ti_2Ni(Nb) matrix, an

enlarged view of area b in (a), S1 and S2 are corresponding SAED results; (c) HRTEM image of the PB between the β-(Ti, Nb) and Ti_2Ni(Nb) phases; (d) BF image of strip structure and corresponding STEM-EDS elemental maps, an enlarged view of area d in (a).

The typical TEM microstructure in Fig. 4 shows details of the multi-layer Ti-23Nb coating, i.e. a polycrystalline microstructure with numerous nanoscale orthogonal acicular precipitates inside the grains. The corresponding SAED pattern, obtained along $[100]_{\beta}$ from area b in Fig. 4a, corresponds to the following orientation relationships: $<100>_{\beta}$ // $<100>_{\alpha''}$ and $\{011\}_{\beta}$ // $\{020\}_{\alpha''}$. An HRTEM image of the coherent interface between α″ and β-matrix is shown in Fig. 4c. The upper-left corner shows the α″ phase, while the lower-right is the β phase. The lattice spacings of the (020) and (00-1) planes of the α″ phase are 0.235 and 0.485 nm, respectively. The interplanar spacing of the (011) plane in the β phase is 0.234 nm. The relationship between the lattice constants of the α″ and β phases is: $a_{\beta} \approx a_{\alpha''} \approx (1/2)^{-1} b_{\alpha''} \approx (1/2)^{-1} c_{\alpha''}$, indicating that the Bain strain between these two phases is very small.

Figure 4d is an enlarged view of area d in Fig. 4a, showing an HRTEM image taken from a grain boundary (GB). The corresponding SAED pattern in Fig. 4e shows the HCP structure viewed along $[0001]_{\alpha'}$. Misfit dislocations are present at the interface of the $\{002\}_{\alpha''}$ and $\{11\text{-}20\}_{\alpha'}$. Thus, the GB is composed of α' phase and two-phase boundaries (α′-α″). Figure 4g presents an HRTEM image of a $\{111\}_{\alpha''}$ twin viewed along $[101]_{\alpha''}$. The {111} twin was further verified by the FFT pattern shown in Fig. 4h.

In addition to the coherent twin boundary (CTB), a $\{020\}_M$ // $\{111\}_T$ (basal-pyramidal, BPy) step can also be observed. The measured angle between the $\{020\}_{\alpha''}$ plane in $\{111\}_{\alpha''}$ twin is ~126°, which is slightly larger than that of $\{10\text{-}11\}_{\alpha}$ twin with 124° [52]. Figure 4i is the corresponding Fourier-filtered HRTEM image of the twin boundary, where the honeycomb structure with an ABCD stacking sequence can be clearly observed along $[101]_{\alpha''}$. Figures 4j-l presents a HAADF-STEM (Z contrast) image with corresponding EDS maps of Ti and Nb. The results illustrate that the Ti content in the α′ lath in the GB (up to 95 at.%, characterized by EDS point analysis) is higher than that in the acicular precipitates embedded in the β matrix, which is consistent with the difference in brightness.

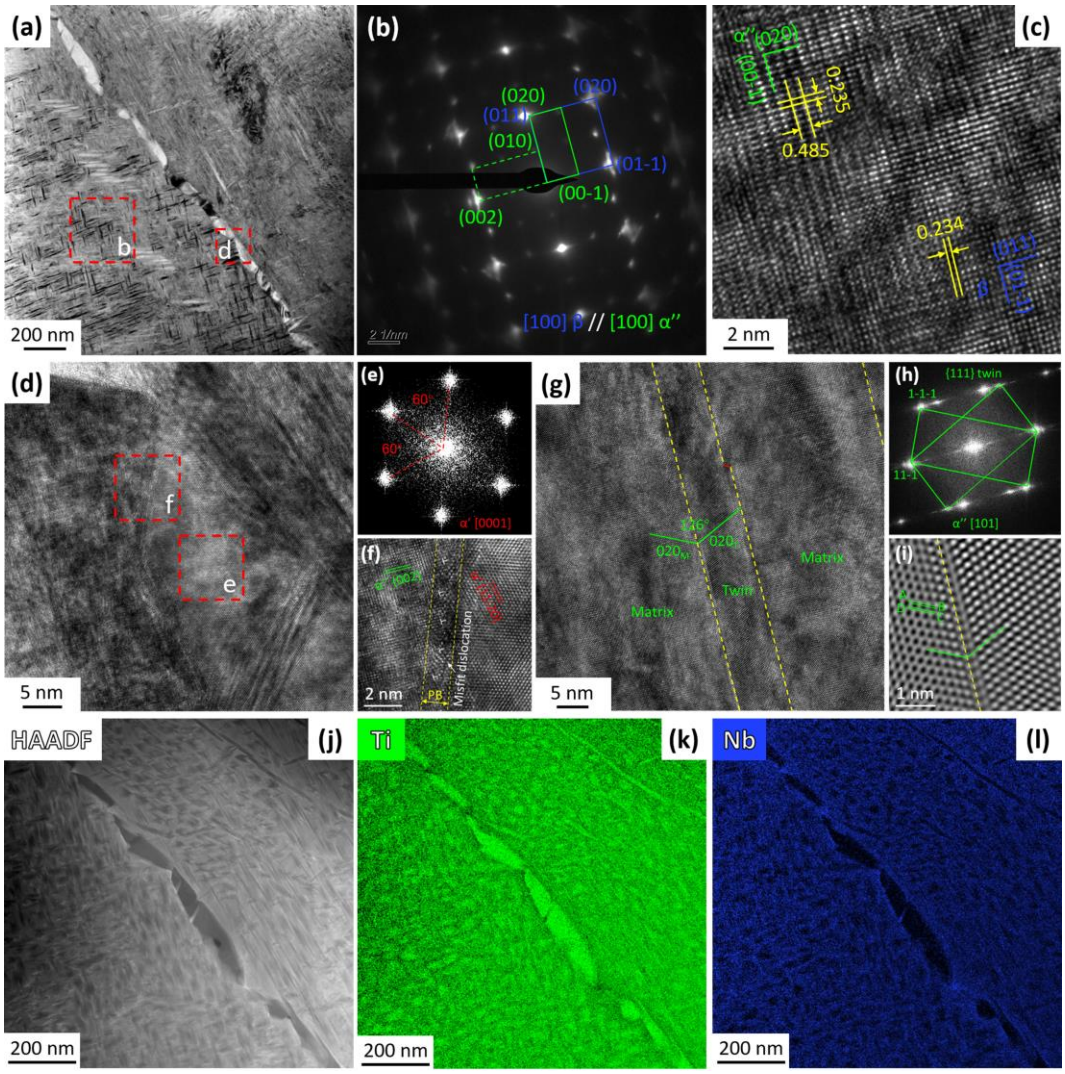

Fig. 4. Typical TEM microstructure of the Ti-23Nb multi-layer coating: (a) BF image; (b) SAED pattern along [100] β taken from area b in (a); (c) HRTEM image along [100] β; (d) HRTEM image taken from the GB, an enlarged view of area d in (a); (e) FFT pattern of area e in (d); (f) an enlarged HRTEM image of area f in (d); (g) HRTEM image of the {111} twin boundary; (h) FFT pattern taken from (g); (i) corresponding Fourier-filtered HRTEM image of the twin boundary; (j) HAADF image and (k-l)corresponding EDS maps.

TEM inspection was used to identify the phase evolution of α″ and β phases within

the grains. The HAADF image and corresponding EDS maps in Fig. 5a-c show clear segregation of Ti and Nb. An EDS scan along the red line shown in Fig. 5a clarifies the specific composition of the α″ and β phases. The Ti content of the α″ phase is about 90 at.%, which is slightly lower than that of α′ phase at the GB (Fig. 4d). The Nb content of the β phase is about 40 at.% (~56.4 wt.%) with a molybdenum equivalency (Mo_{eq}) value of 15 wt.% (>10 wt.%). Thus, the formation of α″ phase is attributed to the lack of Nb caused by the elemental segregation. An HRTEM image of the Ti-rich acicular precipitates and Nb-rich matrix is shown in Fig. 5e. The interface between these two phases is incoherent. The FFT pattern with corresponding Fourier filtered HRTEM images (Fig. 5f and g) shows the typical α″ feature in the Ti-rich zone. The Nb-rich β matrix is confirmed by the FFT pattern (Fig. 5h, taken from Fig. 5e) and corresponding Fourier-filtered HRTEM images (Fig. 5i).

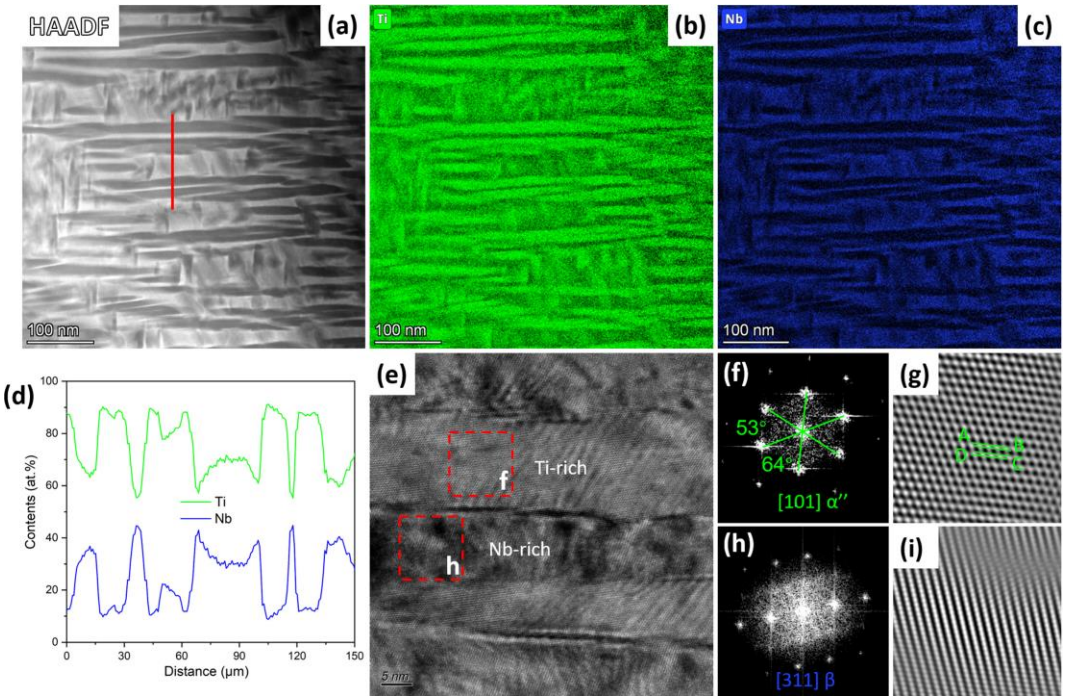

Fig. 5. (a) HAADF image showing the α″ and β phases of the multilayer Ti-23Nb coating; (b-c) corresponding EDS maps; (d) EDS line scan from red line in (a); (e)

HRTEM image of α″ and β phases; (f) and (h) FFT patterns of areas f and h in (e); (g) and (i) corresponding Fourier-filtered HRTEM images.

3.2 Nanoindentation hardness and creep

Typical load-displacement curves of the NiTi substrate, the single-layer and the multi-layer coatings under a 40 mN indentation load are presented in Fig. 6a. The difference in indentation depth and initial unloading contact stiffness among these samples can be easily distinguished. The average nanohardness (H) and reduced Young's modulus (E_r) are shown in Fig. 6b. Compared with the cold-rolled NiTi substrate (H = 4.3 ± 0.4 GPa, E_r =67 ± 4 GPa), which is dominated by the B2 phase, the single-layer coating containing β-(Ti,Nb) exhibits similar nanomechanical behavior (H = 3.9 ± 0.3 GPa, E_r =63 ± 2 GPa). The H and E_r of multi-layer coatings are 3.3 ± 0.2 and 82 ± 4 GPa, respectively.

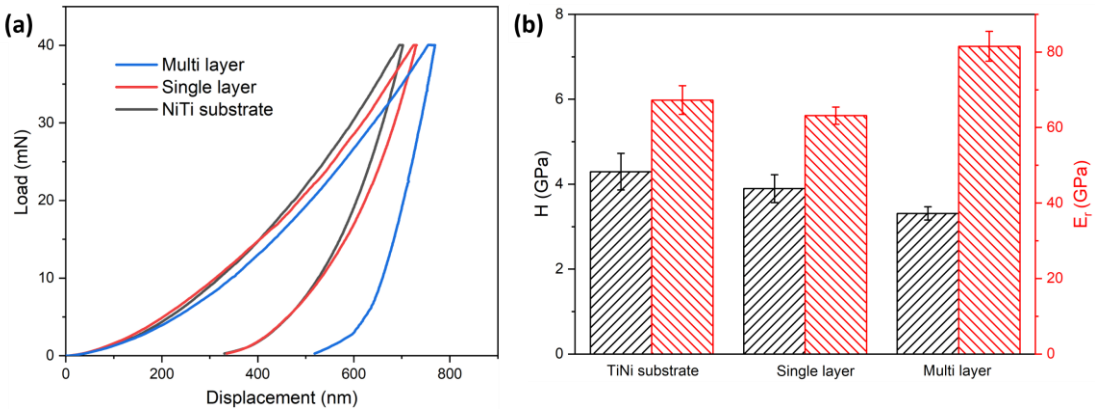

Fig. 6. (a) Load-displacement curves and (b) H and E_r values of the single- and multi-layer coatings and TiNi substrate.

Figure 7a shows typical displacement-time creep curves for the NiTi substrate and the

multi-layer coatings. It is clear that the curves are composed of three parts: loading, creep and unloading zones. Figure 7b is an enlarged view of the creep zone, showing the transition from the initial accelerated creep to the steady-state creep in spite of the fluctuations in displacement. The creep zone curves can be fitted using an empirical formula [53]:

$$h = h_0 + a(t\text{-}t_0)^b + kt \quad (1)$$

where h_0 *and* t_0 are the initial displacement and time, respectively, and a, b, and k are fitting constants. The initial position of the creep zone is set as the origin. Thus, the values of h_0 *and* t_0 are assigned to zero. The depth of multi-layer coating increased sharply after holding for 400 s, indicating two different creep stages. Fitted lines are shown in Fig. 7b. The strain rate $\dot{\varepsilon}$ can be calculated from the ratio of the instantaneous rate h' and h, where the h' is the first derivative of h. The stress (σ) was calculated from the peak load P_{max} divided by the contact area A_c, where A_c is defined as $24.5h^2$, for an ideal Berkovich indenter [54]. Then, the stress exponents n can be calculated by linearly fitting the part of steady-state creep according to formula:

$$n = \frac{\mathrm{d}(\ln\dot{\varepsilon})}{\mathrm{d}(\ln\sigma)} \quad (2)$$

The corresponding logarithmic plots of strain rate versus stress curves are presented in Fig. 7c and 7d. The n values of multi-layer coating and substrate in steady-state are calculated to be ~8.5 and ~5.8, respectively. Besides, the n value of multi-layer coating for stage 1 is ~47.

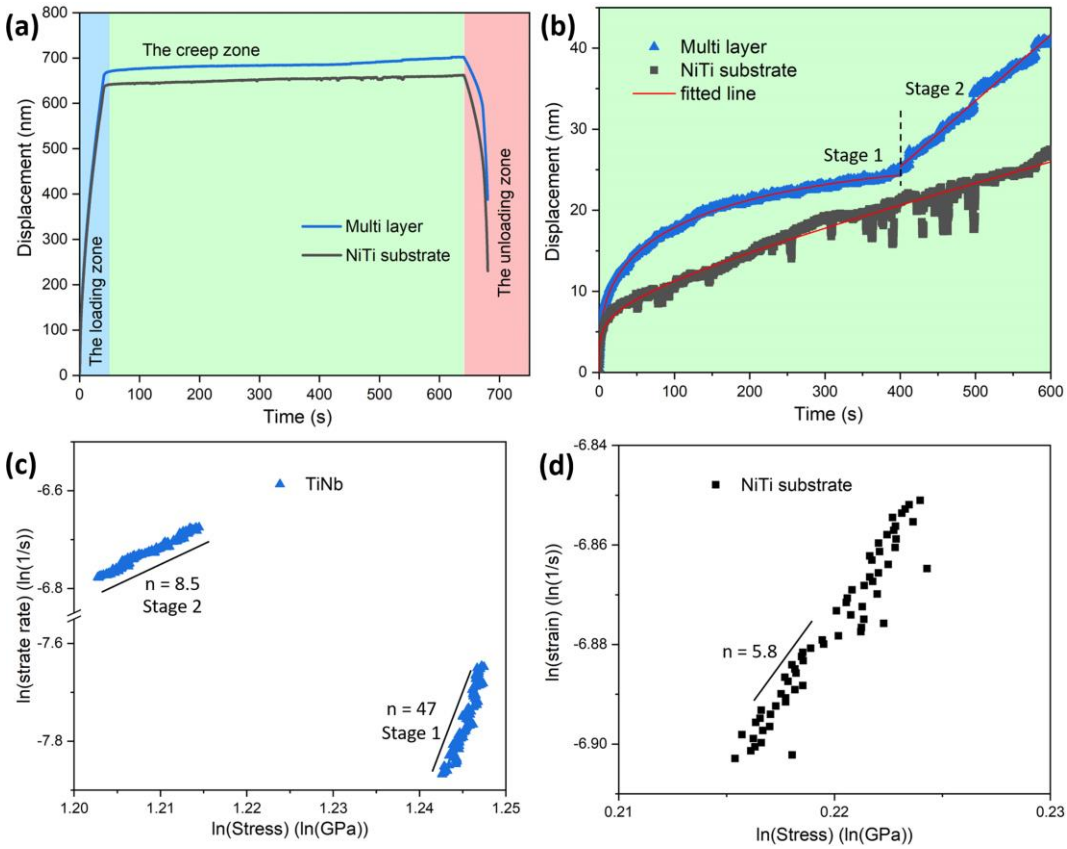

Fig. 7. (a) Creep curves as a function of time (s) for the NiTi substrate and multi-layer coatings; (b) an enlarged view of the creep region in (a) and the corresponding fitted lines; the ln (strain rate) versus ln(stress) plots: (c) multi-layer coating and (d) NiTi substrate.

3.3 Ion release behavior

The release of nickel ions is the critical indicator to measure the biological safety of the alloys. Figure 8 shows the released nickel ion concentration per square centimeter obtained from NiTi substrate, single- and multi-layer coatings immersed in SBF after 1, 7, 14, 21, 28, and 35 days. The highest Ni ion release concentration of the NiTi substrate can be observed at the 14^{th} day, and then it drops to the normal release level (~0.3 mg cm^{-2}) during the subsequent immersion process. Both single- and multi-layer

coatings show good ability to inhibit the release of Ni ions. The Ni ion concentration accumulation for the single-layer coating after the 1st, 7th, 14th, 21th, 28th, and 35th days is reduced by 45%, compared with the ion release concentration from the NiTi substrate. The Ni release rate of these two materials remains ~0.3 mg $cm^{-2}day^{-1}$ without obviously drop after 21 days immersion. For the multi-layer coatings, the release of Ni ions can be reduced up to 62% compared with the NiTi substrate. The release of Ni ions shows a continuous downward trend after 14 days, which was below ~0.2 mg cm^{-2} after 35th days. This impressive suppressed release of Ni ion requires the sacrifice of the mechanical properties, including hardness, Young's modulus, and superelastic properties.

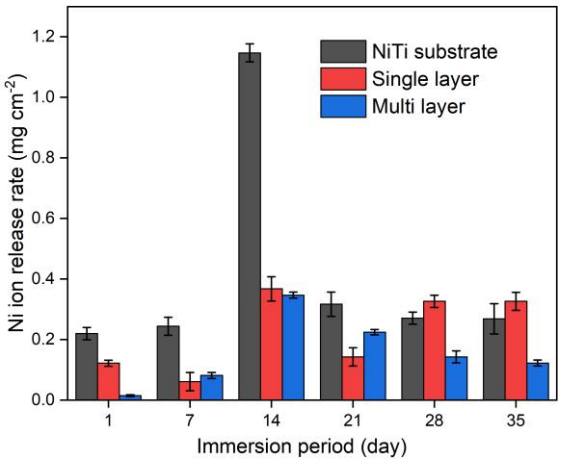

Fig. 8. The concentration of nickel ions released from NiTi substrate, single- and multi-layer coatings after 1, 7, 14, 21, 28, and 35 days of culture.

Figure 9 shows the SE images and corresponding EDS maps of Ti, Nb and Ni for the NiTi substrate, single- and multi-layer coatings. A self-protective calcium phosphate layer with cracks is evident on the surface after 35 days of immersion in SBF solution (310 K). The Ti enrichment located at cracks can be clearly observed. This proves that

the cracks in the calcium phosphate layer can directly reach the substrate. Compared with the NiTi substrate and single-layer coating, the presence of Ni is hardly detected in the multi-layer coating, while a small amount of Nb can be discerned.

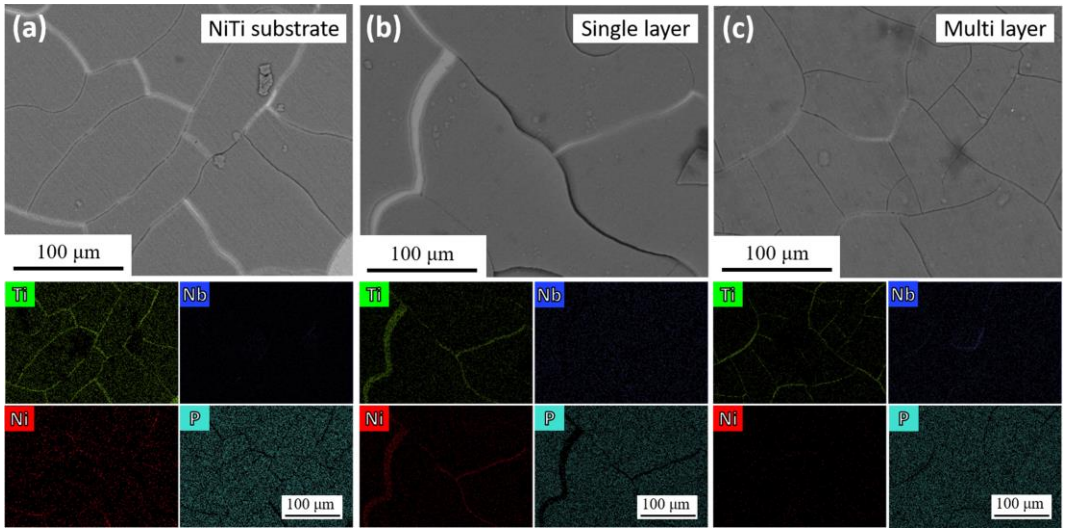

Fig. 9. SE images and corresponding EDS maps of (a) NiTi substrate, (b) single- and (c) multi-layer coatings after 35 days of immersion.

4. Discussion

4.1 Microstructural evolution

It is well accepted that the solidification morphologies and their scales during LMD processing are primarily controlled by the local temperature gradient (G) and solidification rate (R) and can be described by the constitutional supercooling theory [55, 56]. The ratio of G/R determines whether a cellular or dendritic structure forms upon solidification. The bottom region of the molten pool adjacent to the base possesses the highest *G/R,* where the columnar grains dominate. In contrast, the top region is dominated by equiaxed grains, which is consistent with microstructure of the multi-layer coating (Fig. 1d). As for the cellular and dendritic structures in the single-layer

coating (Fig. 1a and c), it is considered as metastable cellular grains, which have been reported in SLM Al-Si [57], CoCrMo [58], and 316L alloys [59]. The GBs of this kind of metastable phase need to be confirmed by electron back-scatter diffraction (EBSD) [60]. Otherwise, columnar grains are difficult to observe using the SEM after polishing and etching.

Due to the rapid movement of incident laser, a strong non-linear and asymmetrically inclined temperature gradient is formed during LMD processing [61, 62]. Such severe melting environments may lead to strong Marangoni convection and turn into complex cellular patterns [63]. The critical condition for the formation of this cellular grain in LMD processing is that the solute(s) becomes immiscible with decreasing temperature [64]. Only in this situation, the solidification behavior is kinetically rather than thermodynamically favored. By ejecting the high-melting temperature solute(s) into liquid phase at the solid-liquid interface, the low melting phase occupies the cell cores and solidifies preferentially. The high-melting phase then solidifies and surrounds the cell cores, thereby forming a eutectic cellular network. Of course, the whole solidification process occurs in the presence of strong convection in the melt pool. The rapid diffusion of Ni during laser melting leads to the formation of different melting points of solute (Nb-rich) and solvent (Ni-rich), which is the fundamental reason for the formation of cellular structure.

The diversity of the microstructure in the eutectic layer and Ni diffusion zone is ascribed to the difference in the number of components in the alloy system during solidification [64]. Once the binary or multicomponent alloy system fails to produce a

binary system of solute (high melting point) and solvent (low melting point) during solidification, the cellular structure dominated by kinetics cannot be formed. In the Ni diffusion zone, since the solute is greater than 1, the extra Nb-rich solute (high melting point) preferentially precipitates as primary β-(Ti, Nb), as shown in Fig. 3b. Then after the remaining melt reaches equilibrium, the eutectic strip structure is formed, see Fig. 3d. Due to the complete miscibility of Ti and Nb, the melt cannot form a binary system by solute segregation [65]. The melt of this unitary system is controlled by thermodynamics in the solidification process. Thus, the top region of the multi-layer Ti-23Nb coating is composed of equiaxed grains, see Fig. 1d.

A schematic of the single- and multi-layer coatings is shown in Fig. 10. For the single-layer coating, the solidification structure is mainly affected by melt convection in the eutectic layer, resulting in a eutectic cellular network composed of β-(Ti, Nb) and NiTi(Nb) phases. In the Ni diffusion zone, the Nb-rich β-(Ti, Nb) phase precipitates and then is surrounded by the Ti_2Ni(Nb) phase with a width of ~250 nm. Away from the Ti_2Ni(Nb) phase, the eutectic strip structure composed of β-(Ti, Nb) and NiTi(Nb) phases can be observed. For the multi-layer coating, the HCP structure (α′) is formed at the prior-β GB and α″ colonies are generated inside the grain, which is due to the difference in the β-stabilization effect caused by the partitioning of Nb.

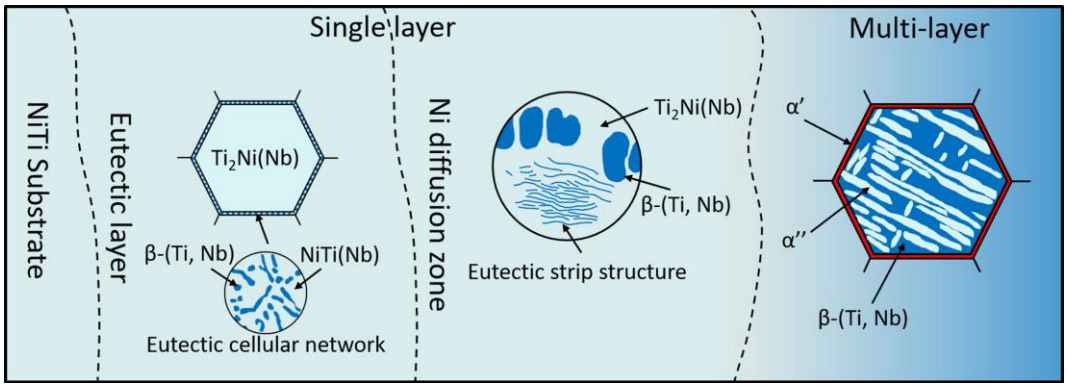

Fig. 10. Schematic of microstructures of the single- and multi-layer coatings

4.2 Mechanical properties analysis

The superior properties in the LMD single-layer coating are attributed to the substantial cellular subgrains and high dislocation density caused by the high cooling rate and Marangoni convection. It has been proven that the evaluated E_r for metastable phases follow the sequence of $E_{\alpha'} > E_{\alpha''} > E_{\beta}$ [66]. Compared to single-layer coatings, the E_r increase of nearly 20 GPa in the multi-layer coating arises from the formation of α′ and α″ phases. The titanium martensite is mainly composed of substitutional supersaturated solid solution with limited strengthening effects. The α′ and α″ phases are even softer than the α phase. In the Ti-Fe binary system, the nanohardness of the α phase is lower than that of the β phase by more than 1 GPa [67]. This means that the stress-induced martensitic transformation can impair the mechanical properties of multi-layer coatings. In addition, it has been proven that the dislocation motion can be pinned by such ultrafine eutectic structures in single-layer coating [60]. These can explain why the hardness of the multi-layer TiNb coating decreases comparing with the single-layer coating.

The elastic recovery (W_e/W_t) and plasticity (W_p/W_t) indices [68] were introduced to further clarify the deformation behavior of materials, as shown in Fig. 11a. The value of W_e/W_t represents the energy released by the materials after unloading, while the value of W_p/W_t represents the energy absorbed. They reflect the deformation tendency of materials after being loaded. For NiTiNb superelastic alloys, high W_e/W_t values indicate that the material has excellent elastic recovery ability. In general, the E_r of materials is related to their H. The high E_r denotes good elastic recovery ability. The relatively lower hardness in the multi-layer coatings reduces its elastic recovery ability, compared with NiTi substrate and single-layer coatings. In addition, H/E_r (the elastic strain to failure) and H^3/E_r^2 (the yield pressure) are able to evaluate the anti-wear behavior of materials effectively [69]. It should be noted that the indicator of H/E_r is not applicable in ceramic and amorphous materials [70]. Despite their high H/E_r values, they appear to be brittle because of the covalent bonds. But this indicator is applicable for alloys, where a high value of H/E_r and H^3/E_r^2 indicate good anti-wear properties. The values of H/E_r and H^3/E_r^2 are shown in Fig. 11b. The multi-layer coating with low hardness and high modulus shows the worst wear properties. This means that except for the high Nb content ($Mo_{eq} \geq 10$ wt.%) in the LMD Ti-xNb multi-layer coating, the lack of Nb in nano-scale caused by segregation should also be considered.

Based on the recent work by Wang et al. [49], the indentation depths (including maximum indentation depth, h_{max}, residual depth during unloading, h_r, superelastic recovery depth, h_{sr}, and elastic recovery depth, h_{er}) are introduced here to reflect the deformation behavior at various stages, as shown in Fig. 11c. Figure 11d shows the

calculated values of total strain recovery (η_r), superelastic strain recovery (η_{sr}) and elastic strain recovery (η_{er}). The relationship among them follows the equation as $\eta_r = \eta_{sr} + \eta_{er}$. The value of η_r in the multi-layer coating is relatively low (0.31 ± 0.2), showing the same trend as W_e/W_t. The advantage of this method is that it can conveniently characterize the superelastic behavior of the material. It is clear that the single-layer coating maintains the same superelastic behavior as the NiTi substrate. The values of η_{sr} in both NiTi substrate and single-layer coating are higher than those of η_{er}, indicating that the superelastic behavior is dominant in the whole elastic recovery behavior. While the loss of the superelastic behavior of the multi-layer coating can be observed in Fig. 11d, which might be the major reason for the reduction of η_r.

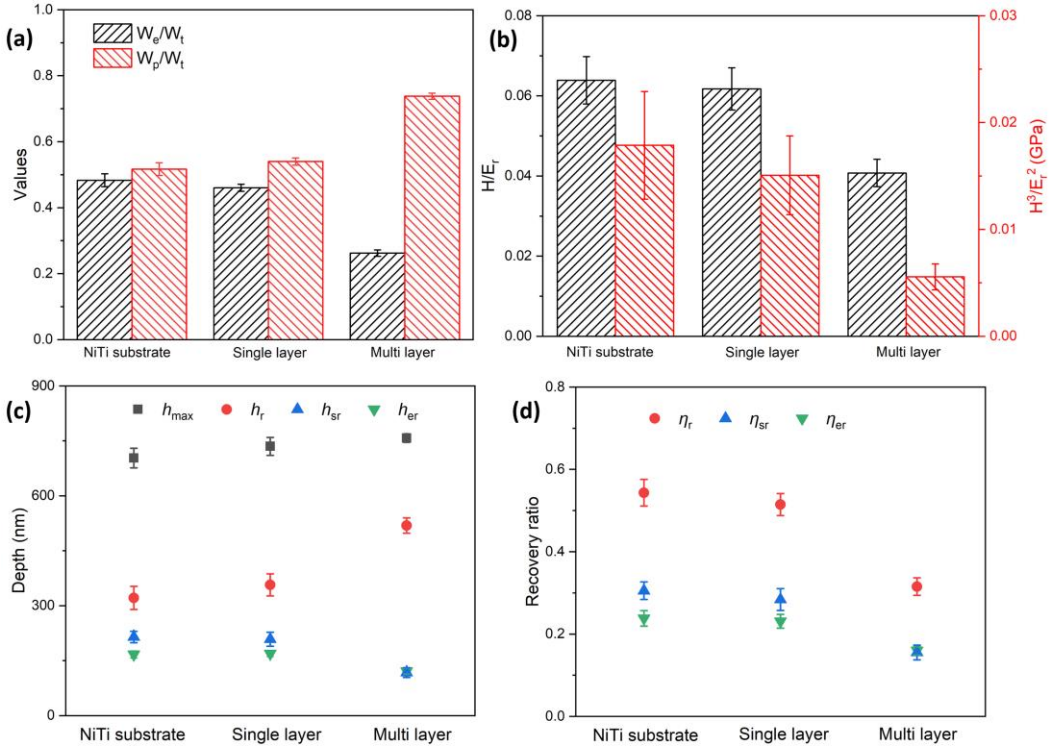

Fig.11 (a) Elastic recovery (W_e/W_t) and plasticity (W_p/W_t) indices; (b) the values of H/E_r and H^3/E_r^2; (c) indentation depths (maximum indentation depth h_{max}, residual depth during unloading h_r, superelastic recovery depth h_{sr} and elastic recovery depth h_{er}); (d)

the values of total strain recovery (η_r), superelastic strain recovery (η_{sr}) and elastic strain recovery (η_{er}).

Pressing of indenter tip into the materials surface can exaggerate the local strain/stress gradient, leading to the formation of dislocation-mediated plastic deformation. The martensitic transformation is activated in the adjacent region owing to the transfer of the strain/stress field. At this time (initial stage), the creep behavior is dominated by dislocation-mediated plastic deformation. As the creep further progresses, the large dislocation density caused by the incipient high strain rate decreases rapidly until it enters the steady-state creep stage. It is well-known that the creep mechanism can be determined by the value of n. The dominant creep mechanism is controlled by atomic diffusion for $n = 1$, GB sliding for $n \approx 2$, and dislocation movement for $n > 3$ [71]. The n values of the NiTi substrate and multi-layer coating are higher than 3, indicating that the creep mechanism is mainly governed by the movement of dislocations. The second-stage creep phenomenon is probably due to the dislocation annihilation. Due to the high cooling rate, the high density of misfit dislocations and geometrically-necessary dislocations (GNDs, induced by internal stress) in LMD materials are inevitable and inherent [72]. Such high dislocation densities might be reduced through slip annihilation in the long period of creep, resulting in dynamic softening [73, 74].

4.3 Ion release analysis

The calcium phosphate layer can effectively inhibit the release of Ni ions for 14 days (Fig. 8). Once the local stress induced by the difference in linear expansion coefficient is greater than the yield stress, several cracks form on the calcium phosphate layer. Combined with the EDS mapping results, the local exposure of alloys is considered as the main reason for the surge of Ni ion release on the 14^{th} day. Although the convection of the molten pool can accelerate the diffusion, the content of Ni in the single-layer coating is still lower than that of the NiTi substrate [50]. In addition, little Ni can be observed in the multi-layer coating. Thus, the absence of Ni near the outer surface of the multi-layered coating can physically prevent the Ni ion release.

5. Conclusions

Single- and multi-layer Ti-23Nb coatings have been successfully produced on a NiTi substrate by LMD processing. The coatings showed promising results in retaining the superelasticity of the substrate and reducing toxic Ni ion release. The main conclusions from the study are:

1. The single-layer coating has a cellular structure in the eutectic layer, i.e. β-(Ti,Nb) and NiTi(Nb) phases, strip structure, and prior β-(Ti, Nb) surrounded by Ti_2Ni(Nb) in Ni diffusion zone. The multi-layer coating is composed of α′, α″, and prior β phases due to the partition of Nb and the lack of Ni diffusion.

2. The single-layer coating containing β-(Ti,Nb) exhibits similar nanomechanical behavior to the cold-rolled NiTi substrate, including the nanohardness (H, ~4.0 GPa), the reduced Young's modulus (E_r, ~65 GPa), the elastic strain to failure (H/E_r, ~0.06),

the yield stress (H^3/E_r^2, ~0.016 GPa), and the superelastic strain recovery (η_{sr}, ~0.3).

3. The formation of α' and α" in the multi-layer coating degrades the mechanical properties, including the hardness (H, ~3.3 GPa), the Young's modulus (E_r, ~82 GPa), the anti-wear (H/E_r, ~0.04; H^3/E_r^2, ~0.005 GPa), and the superelasticity (η_{sr}, ~0.16).

4. The stress exponents of the cold-rolled NiTi substrate and LMD coating indicate that the creep behavior is controlled by the dislocation movement. The LMD coating exhibits the better creep resistance than the NiTi substrate.

5. Upon initial immersion, a protective calcium phosphate layer is formed that inhibits the release of Ni ion. Compared with the ion release concentration of the NiTi substrate, the Ni ion concentration accumulation of single- and multi-layer coatings in 1^{st}, 7^{th}, 14^{th}, 21^{th}, 28^{th}, and 35^{th} days is reduced by 45% and 62%, respectively.

Acknowledgments

This research was supported by the National Natural Science Foundation of China (Grant No. 52071346) and Natural Science Foundation of Hunan Province, China (Grant No. 2021JJ30846). The authors would also thank Sinoma Institute of Materials Research (Guang Zhou) Co., Ltd. for the assistance with the TEM characterization.

Reference

[1] J. Scheinpflug, M. Pfeiffenberger, A. Damerau, F. Schwarz, M. Textor, A. Lang, F. Schulze, Journey into bone models: a review, Genes 9(5) (2018) 247.

[2] A. Tamoud, F. Zaïri, A. Mesbah, F. Zaïri, Modeling multiaxial damage regional variation in human annulus fibrosus, Acta Biomaterialia 136 (2021) 375-388.

[3] S.M. Haddock, O.C. Yeh, P.V. Mummaneni, W.S. Rosenberg, T.M. Keaveny, Similarity in the fatigue behavior of trabecular bone across site and species, Journal of Biomechanics 37(2) (2004) 181-187.

[4] A.H. Burstein, D.T. Reilly, M. Martens, Aging of bone tissue: mechanical properties, The Journal of bone and joint surgery. American volume 58(1) (1976) 82-86.

[5] J. Li, H. Gong, Fatigue behavior of cortical bone: a review, Acta Mechanica Sinica 37(3) (2021) 516-526.

[6] M.J. Rouhani, H. Abboudi, N. Gibbons, T. El-Husseiny, Endourologic management of an iatrogenic ureteral avulsion using a thermoexpandable nickel-titanium alloy stent (Memokath 051), Journal of endourology case reports 3(1) (2017) 57-60.

[7] Y. Wang, D. Xia, X. Luo, H. Zhang, J. Wu, P. Zhou, S. Xu, Comparison of the Kirschner Wire Tension Band with a Novel Nickel–Titanium Arched Shape-Memory Alloy Connector in Transverse Patellar Fractures: A Retrospective Study, The journal of knee surgery 34(09) (2021) 987-996.

[8] R. Tabola, R. Cirocchi, A. Fingerhut, A. Arezzo, J. Randolph, V. Grassi, G.A. Binda, V. D'Andrea, I. Abraha, G. Popivanov, A systematic analysis of controlled clinical trials using the NiTi CAR™ compression ring in colorectal anastomoses, Techniques in coloproctology 21(3) (2017) 177-184.

[9] S. Buxton, E. Garman, K.E. Heim, T. Lyons-Darden, C.E. Schlekat, M.D. Taylor, A.R. Oller, Concise review of nickel human health toxicology and ecotoxicology, Inorganics 7(7) (2019) 89.

[10] P. Chantarawaratit, T. Yanisarapan, Exposure to the oral environment enhances the corrosion of metal orthodontic appliances caused by fluoride-containing products: Cytotoxicity, metal ion release, and surface roughness, American Journal of Orthodontics and Dentofacial Orthopedics 160(1) (2021) 101-112.

[11] S.K. Chowdhury, V. Nagarjuna, B. Bhaskar, Metallic Biomaterials in Tissue Engineering: Retrospect and Prospects, Biomaterials in Tissue Engineering and Regenerative Medicine, (2021) 19-60.

[12] H. Shi, W. Zhao, X. Wei, Y. Ding, X. Shen, W. Liu, Effect of Ti addition on mechanical properties and corrosion resistance of Ni-free Zr-based bulk metallic glasses for potential biomedical applications, Journal of Alloys and Compounds 815 (2020) 152636.

[13] A. Ramezannejad, W. Xu, W. Xiao, K. Fox, D. Liang, M. Qian, New insights into nickel-free superelastic titanium alloys for biomedical applications, Current Opinion in Solid State and Materials Science 23(6) (2019) 100783.

[14] M. Lai, Y. Gao, B. Yuan, M. Zhu, Indirect determination of martensitic transformation temperature of sintered nickel-free Ti-22Nb-6Zr alloy by low temperature compression test, Materials & Design 60 (2014) 193-197.

[15] Y. Al-Zain, H.Y. Kim, H. Hosoda, T.H. Nam, S. Miyazaki, Shape memory properties of Ti-Nb-Mo biomedical alloys, Acta Materialia 58(12) (2010) 4212-4223.

[16] S. Li, Y.W. Kim, M.S. Choi, T.H. Nam, Achieving high porosity and large recovery strain in Ni-free high Zr-containing Ti-Zr-based shape memory alloy scaffolds by fiber metallurgy, Intermetallics 128(3) (2021) 107015.

[17] H. Kim, Y. Ikehara, J.I. Kim, H. Hosoda, S. Miyazaki, Martensitic transformation, shape memory

effect and superelasticity of Ti-Nb binary alloys, Acta materialia 54(9) (2006) 2419-2429.
[18] Duerig T W, Melton K N, Stöckel D. Engineering aspects of shape memory alloys. Butterworth-heinemann, 2013.
[19] H. Wang, F. Liu, X. Xiong, S. Ke, X. Zeng, P. Lin, Structure, corrosion resistance and in vitro bioactivity of Ca and P containing TiO_2 coating fabricated on NiTi alloy by plasma electrolytic oxidation, Applied Surface Science 356(30) (2015) 1234-1243.
[20] C. Yan, G. Ma, A. Chen, Y. Chen, J. Wu, W. Wang, S. Yang, Y. Shi, Additive manufacturing of hydroxyapatite and its composite materials: A review, Journal of Micromechanics and Molecular Physics 5(3) (2020) 203002.
[21] Y. Say, B. Aksakal, Enhanced corrosion properties of biological NiTi alloy by hydroxyapatite and bioglass based biocomposite coatings, Journal of Materials Research and Technology 9(2) (2020) 1742-1749.
[22] A. Mehrvarz, Y. Ghazanfar-Ahari, J. Khalil-Allafi, S. Mahdavi, M. Etminanfar, The microstructural features and corrosion behavior of Hydroxyapatite/ZnO nanocomposite electrodeposit on NiTi alloy: Effect of current density, Ceramics International 48(2) (2022) 2191-2202.
[23] N. Gangil, A.N. Siddiquee, S. Maheshwari, Towards applications, processing and advancements in shape memory alloy and its composites, Journal of Manufacturing Processes 59 (2020) 205-222.
[24] S. Liu, S. Han, L. Wang, J. Liu, H. Tang, Effects of Nb on the microstructure and compressive properties of an As-Cast Ni44Ti44Nb12 eutectic alloy, Materials 12(24) (2019) 4118.
[25] S. Liu, S. Han, L. Zhang, L.-Y. Chen, L. Wang, L. Zhang, Y. Tang, J. Liu, H. Tang, L.C. Zhang, Strengthening mechanism and micropillar analysis of high-strength NiTi-Nb eutectic-type alloy prepared by laser powder bed fusion, Composites Part B: Engineering 200 (2020) 108358.
[26] S. Liu, J. Liu, L. Wang, R.L. Ma, Y. Zhong, W. Lu, L.C. Zhang, Superelastic behavior of in-situ eutectic-reaction manufactured high strength 3D porous NiTi-Nb scaffold, Scripta Materialia 181 (2020) 121-126.
[27] S. Liu, W. Liu, J. Liu, J. Liu, L. Zhang, Y. Tang, L.C. Zhang, L. Wang, Compressive properties and microstructure evolution in NiTiNb alloy with mesh eutectic phase, Materials Science and Engineering: A 801 (2021) 140434.
[28] X. Lan, H. Wu, Y. Liu, W. Zhang, R. Li, S. Chen, X. Zai, T. Hu, Microstructures and tribological properties of laser cladded Ti-based metallic glass composite coatings, Materials Characterization 120 (2016) 82-89.
[29] H. Wu, L. Liang, X. Lan, Y. Yin, M. Song, R. Li, Y. Liu, H. Yang, L. Liu, A. Cai, Tribological and biological behaviors of laser cladded Ti-based metallic glass composite coatings, Applied Surface Science 507 (2020) 145104.
[30] Y. Yang, Y. Ren, Y. Tian, K. Li, L. Bai, Q. Huang, Q. Shan, Y. Tian, H. Wu, Microstructure and tribological behaviors of $FeCoCrNiMoSi_x$ high-entropy alloy coatings prepared by laser cladding, Surface and Coatings Technology 432 (2021) 128009.
[31] J. Li, M. Su, G. Li, L. Liu, Atomic structure revolution and excellent performance improvement of composites induced by laser ultrafine-nano technology, Composites Part B: Engineering 185 (2020) 107792.
[32] S. Sui, Y. Chew, Z. Hao, F. Weng, C. Tan, Z. Du, G. Bi, Effect of cyclic heat treatment on the microstructure and mechanical properties of laser aided additive manufacturing Ti-6Al-2Sn-4Zr-2Mo alloy, Advanced Powder Materials 1(1) (2022) 100002.
[33] J.e. Sun, B. Zhang, X. Qu, High strength Al alloy development for laser powder bed fusion, Journal

of Micromechanics and Molecular Physics (2021) 2141001.
[34] Y. Han, L. Wang, K. Liu, W. Yan, Numerical modeling of laser powder bed fusion of metallic glasses: Prediction of crystallization, Journal of Micromechanics and Molecular Physics 5(4) (2020) 2050013.
[35] T. Zhang, C.T. Liu, Design of titanium alloys by additive manufacturing: A critical review, Advanced Powder Materials 1(1) (2022) 100014.
[36] M. He, Y. Ni, S. Wang, On the microstructure and tensile properties of Inconel 718 alloy fabricated by selective laser melting and conventional casting, Journal of Micromechanics and Molecular Physics (2021) 2141003.
[37] L. Ren, W. Xiao, C. Ma, R. Zheng, L. Zhou, Development of a high strength and high ductility near β-Ti alloy with twinning induced plasticity effect, Scripta Materialia 156 (2018) 47-50.
[38] Q. Wang, C. Han, T. Choma, Q. Wei, C. Yan, B. Song, Y. Shi, Effect of Nb content on microstructure, property and in vitro apatite-forming capability of Ti-Nb alloys fabricated via selective laser melting, Materials & Design 126 (2017) 268-277.
[39] S. Huang, R.L. Narayan, J.H.K. Tan, S.L. Sing, W.Y. Yeong, Resolving the porosity-unmelted inclusion dilemma during in-situ alloying of Ti34Nb via laser powder bed fusion, Acta Materialia 204 (2021) 116522.
[40] J. Wang, W. Xiao, L. Ren, Y. Fu, C. Ma, The roles of oxygen content on microstructural transformation, mechanical properties and corrosion resistance of Ti-Nb-based biomedical alloys with different β stabilities, Materials Characterization 176 (2021) 111122.
[41] J. Zhang, B. Song, C. Cai, L. Zhang, Y. Shi, Tailorable microstructure and mechanical properties of selective laser melted TiB/Ti-6Al-4V composite by heat treatment, Advanced Powder Materials 1(2) (2022) 100010.
[42] X.Y. Zhang, G. Fang, S. Leeflang, A.J. Böttger, A.A. Zadpoor, J. Zhou, Effect of subtransus heat treatment on the microstructure and mechanical properties of additively manufactured Ti-6Al-4V alloy, Journal of Alloys and Compounds 735 (2018) 1562-1575.
[43] W. Xu, M. Brandt, S. Sun, J. Elambasseril, Q. Liu, K. Latham, K. Xia, M. Qian, Additive manufacturing of strong and ductile Ti-6Al-4V by selective laser melting via in situ martensite decomposition, Acta Materialia 85 (2015) 74-84.
[44] H. Fan, Y. Liu, S. Yang, Martensite decomposition during post-heat treatments and the aging response of near-α Ti-6Al-2Sn-4Zr-2Mo (Ti-6242) titanium alloy processed by selective laser melting (SLM), Journal of Micromechanics and Molecular Physics (2021) 2050018.
[45] P. Kürnsteiner, M.B. Wilms, A. Weisheit, B. Gault, E.A. Jägle, D. Raabe, High-strength Damascus steel by additive manufacturing, Nature 582(7813) (2020) 515-519.
[46] E. Yamamoto, R.P. Crawford, D.D. Chan, T.M. Keaveny, Development of residual strains in human vertebral trabecular bone after prolonged static and cyclic loading at low load levels, Journal of biomechanics 39(10) (2006) 1812-1818.
[47] Z. Xu, H. Zhang, W. Li, A. Mao, L. Wang, G. Song, Y. He, Microstructure and nanoindentation creep behavior of CoCrFeMnNi high-entropy alloy fabricated by selective laser melting, Additive Manufacturing 28 (2019) 766-771.
[48] Y. Ren, L. Liang, Q. Shan, A. Cai, J. Du, Q. Huang, S. Liu, X. Yang, Y. Tian, H. Wu, Effect of volumetric energy density on microstructure and tribological properties of FeCoNiCuAl high-entropy alloy produced by laser powder bed fusion, Virtual and Physical Prototyping 15(S1) (2020) 543-554.
[49] L. Wang, L. Xie, Y. Lv, L.C. Zhang, L. Chen, Q. Meng, J. Qu, D. Zhang, W. Lu, Microstructure evolution and superelastic behavior in Ti-35Nb-2Ta-3Zr alloy processed by friction stir processing, Acta

Materialia 131 (2017) 499-510.
[50] J. Hu, Y. Ren, Q. Huang, H. He, L. Liang, J. Liu, R. Li, H. Wu, Microstructure and Corrosion Behavior of Ti-Nb Coatings on NiTi Substrate Fabricated by Laser Cladding, Coatings 11(5) (2021) 597.
[51] G. Pharr, W.C. Oliver, F. Brotzen, On the generality of the relationship among contact stiffness, contact area, and elastic modulus during indentation, Journal of materials research 7(3) (1992) 613-617.
[52] B. Wei, S. Ni, Y. Liu, M. Song, Stress accommodation by α to α ″transformation at the {10-11} twin boundary in a cold-rolled Ti-5at.% Al alloy, Materialia 8 (2019) 100469.
[53] W. He, Q. Zeng, C. Yan, J. Zhu, J. Cao, Loading rate and holding load dependent room temperature nanoindentation creep behavior of 60NiTi alloy: individual and coupling effects, Journal of Materials Science and Technology 101 (2022) 173-186.
[54] A. Ataee, Y. Li, C. Wen, A comparative study on the nanoindentation behavior, wear resistance and in vitro biocompatibility of SLM manufactured CP-Ti and EBM manufactured Ti64 gyroid scaffolds, Acta biomaterialia 97 (2019) 587-596.
[55] W. Jiang, W. Yu, J. Li, Z. You, C. Li, X. Lv, Segregation and morphological evolution of Si phase during electromagnetic directional solidification of hypereutectic Al-Si alloys, Materials 12(1) (2019) 10.
[56] H. Li, Y. Huang, S. Jiang, Y. Lu, X. Gao, X. Lu, Z. Ning, J. Sun, Columnar to equiaxed transition in additively manufactured CoCrFeMnNi high entropy alloy, Materials & Design 197 (2021) 109262.
[57] H. Wu, Y. Ren, J. Ren, L. Liang, R. Li, Q. Fang, A. Cai, Q. Shan, Y. Tian, I. Baker, Selective laser melted AlSi10Mg alloy under melting mode transition: Microstructure evolution, nanomechanical behaviors and tensile properties, Journal of Alloys and Compounds 873 (2021) 159823.
[58] M. Zhang, Y. Yang, C. Song, Y. Bai, Z. Xiao, An investigation into the aging behavior of CoCrMo alloys fabricated by selective laser melting, Journal of Alloys and Compounds 750 (2018) 878-886.
[59] C. Zhao, Y. Bai, Y. Zhang, X. Wang, J.M. Xue, H. Wang, Influence of scanning strategy and building direction on microstructure and corrosion behaviour of selective laser melted 316L stainless steel, Materials & Design 209 (2021) 109999.
[60] B. Chen, S. Moon, X. Yao, G. Bi, J. Shen, J. Umeda, K. Kondoh, Strength and strain hardening of a selective laser melted AlSi10Mg alloy, Scripta Materialia 141 (2017) 45-49.
[61] Z. Luo, Y. Zhao, A survey of finite element analysis of temperature and thermal stress fields in powder bed fusion additive manufacturing, Additive Manufacturing 21 (2018) 318-332.
[62] M. Froend, F.E. Bock, S. Riekehr, N. Kashaev, B. Klusemann, J. Enz, Experimental investigation of temperature distribution during wire-based laser metal deposition of the Al-Mg alloy 5087, Materials Science Forum, Trans Tech Publ, 2018, 988-994.
[63] A. Mizev, D. Schwabe, Convective instabilities in liquid layers with free upper surface under the action of an inclined temperature gradient, Physics of Fluids 21(11) (2009) 112102.
[64] K. Prashanth, J. Eckert, Formation of metastable cellular microstructures in selective laser melted alloys, Journal of Alloys and Compounds 707 (2017) 27-34.
[65] Z. He, Z. Wang, W. Wang, A. Fan, Z. Xu, Surface modification of titanium alloy Ti6Al4V by plasma niobium alloying process, Surface and Coatings Technology 201(9-11) (2007) 5705-5709.
[66] J.J. Gutiérrez Moreno, D. Papageorgiou, G. Evangelakis, C.E. Lekka, An ab initio study of the structural and mechanical alterations of Ti-Nb alloys, Journal of Applied Physics 124(24) (2018) 245102.
[67] A. Ju, A. Tt, A. Tt, A. Sk, A. Jf, A. Hn, B. Ys, C. Js, A. Kk, Microstructures analysis and quantitative strengthening evaluation of powder metallurgy Ti-Fe binary extruded alloys with (α+β)-dual-phase, Materials Science and Engineering: A 803 (2021) 140708.
[68] G.N. Mekgwe, O.J. Akinribide, S.O. Akinwamide, P.A. Olubambi, Fabrication of graphite

reinforced TiCxNy by spark plasma sintering technique: A comparative assessment of microstructural integrity and nanoindentation properties, Vacuum 187 (2021) 110144.
[69] H. Wu, Y. Ren, J. Ren, A. Cai, M. Song, Y. Liu, X. Wu, Q. Li, W. Huang, X. Wang, Effect of melting modes on microstructure and tribological properties of selective laser melted AlSi10Mg alloy, Virtual and Physical Prototyping 15(S1) (2020) 570-582.
[70] W. Zhai, L. Bai, R. Zhou, X. Fan, K. Zhou, Recent Progress on Wear-Resistant Materials: Designs, Properties, and Applications, Advanced Science 8(11) (2021) 2003739.
[71] J. Hu, Z. Wei, G. Bi, J. Lu, W. Huo, Y. Zhang, Nanoindentation creep behavior of coarse-grained and ultrafine-grained pure magnesium and AZ31 alloy, Materials Science and Engineering: A 698 (2017) 348-355.
[72] Z. Li, Z. Li, Z. Tan, D.-B. Xiong, Q. Guo, Stress relaxation and the cellular structure-dependence of plastic deformation in additively manufactured AlSi10Mg alloys, International Journal of Plasticity 127 (2020) 102640.
[73] Y. Lu, R. Chen, Y. Wang, Z. Chen, Phase-field crystal study of topological evolution during grain annihilation process in polycrystalline materials, Physica B: Condensed Matter 622 (2021) 413363.
[74] N.B. Burbery, G. Po, R. Da S, N. Ghoniem, W.G. Ferguson, Dislocation dynamics in polycrystals with atomistic-informed mechanisms of dislocation-grain boundary interactions, Journal of Micromechanics & Molecular Physics 02(01) (2017) 1750003.